Anomalous diffusion in quasi-geostrophic flow

J. S. Urbach[2], E. R. Weeks[1], and Harry L. Swinney[1]

[1] Center for Nonlinear Dynamics and Department of Physics, University of Texas at Austin, Austin, TX 78712, USA
[2] Department of Physics, Georgetown University, Washington, DC 20057, USA

Abstract. We review a series of experimental investigations of anomalous transport in quasi-geostrophic flow. Tracer particles are tracked for long periods of time in two-dimensional flows comprised of chains of vortices generated in a rapidly rotating annular tank. The tracer particles typically follow chaotic trajectories, alternately sticking in vortices and flying long distances in the jets surrounding the vortices. Probability distribution functions (PDFs) are measured for the sticking and flight times. The flight PDFs are found to be power laws for most time-dependent flows with coherent vortices. In many cases the PDFs have a divergent second moment, indicating the presence of Lévy flights. The variance of an ensemble of particles is found to vary in time as $\sigma^2 \sim t^\gamma$, with $\gamma > 1$ (superdiffusion). The dependence of the variance exponent γ on the flight and sticking PDFs is studied and found to be consistent with calculations based on a continuous time random walk model.

1 Introduction

An ensemble of particles in a non-uniform fluid flow will disperse as a consequence of the variations in the fluid velocity as well as the effects of molecular diffusion. In most situations, advection due to fluid motion is much faster than molecular diffusion, and dominates the transport process. Coherent large scale structures, such as vortices and jets, are frequently present in fluid flows and strongly influence particle motion. A quantitative understanding of the effect of coherent structures on transport and mixing in fluids is essential to accurately model such diverse processes as the dispersal of pollutants in the ocean and atmosphere, the persistence of the atmospheric ozone hole, and mixing and chemical reactions in stirred fluids.

Coherent structures typically result in inhomogeneous transport, with particles mixing well in some regions of the flow but isolated from others. An example of this phenomenon is the maintenance of the ozone hole by the circumpolar night jet. Similarly, Jupiter's Great Red Spot stays red despite the extremely turbulent environment because the existence of a stable vortex inhibits turbulent mixing.

The presence of coherent structures results in correlations in particle motion that can persist for long distances and/or times. This may result in the inapplicability of the Central Limit Theorem used to derive the equation for the dispersion of particles in a normal diffusive process, $\sigma^2 = \langle x^2 \rangle - \langle x \rangle^2 \sim t$, often resulting instead in anomalous diffusion, $\sigma^2 \sim t^\gamma, \gamma \neq 1$ [1]. The presence

of anomalous diffusion in the atmosphere was recognized in 1926 by Richardson [2], who investigated the separation of weather balloons and found in some circumstances $\sigma^2 \sim t^3$. (At very long times, transport in fluids of finite extent will necessarily be normally diffusive due to Brownian motion [3]. In many realistic flows, however, there are several orders of magnitude between the time scale for mixing due to advection and that due to Brownian motion.)

In this paper we review transport studies performed in a two dimensional (2D) flow. The study of 2D flows is of interest in part because its relative simplicity facilitates comparison between theory and experiment. In addition, most atmospheric and other geophysical flows are often predominantly 2D as a result of the effect of planetary rotation or stratification, as are some flows of importance in plasma physics from the effects of applied magnetic fields. Finally, the equations of motion for tracer particles in a 2D flow are identical to Hamilton's equations of motion in phase space for dynamical systems [4], so 2D fluid flow provides a unique avenue for investigating Hamiltonian chaos.

The experiments described below were performed in a rotating annulus designed to match the important dimensionless parameters of large scale geophysical flows. Rapid rotation ensures a predominantly 2D flow, as predicted by the Taylor-Proudman theorem [5]. A schematic of the annulus is shown in Fig. 1. The annulus is completely filled with fluid. The top and sides are transparent to allow for illumination and visualization. The flow is forced by pumping fluid into and out of the annulus through concentric rings of holes in the base of the annulus. The pumping generates a radial pressure gradient which, through the action of the coriolis force, generates an azimuthal jet, co-rotating when the source ring lies outside the sink ring, and counter-rotating for the opposite configuration. The bottom of the annulus has a slope of 0.1, which mimics the dynamical effect of planetary curvature on atmospheric flows (the beta-effect) [5]. A discussion of the design considerations for the annulus can be found in [6].

2 Transport at high Reynolds number

Experiments investigating the dynamics of strongly nonlinear geostrophic flow are described in Refs. [6-8]. In addition to quantitative studies of the dynamical instabilities, qualitative studies of mixing and transport were performed by dye injection. For westward (counter-rotating) jets, large coherent vortices were found to persist in a turbulent background over a wide range of flow parameters. Dye injected into the vortices remained inside the vortex for long periods of time, while dye injected outside of the vortex mixed rapidly throughout the turbulent flow, but would not significantly penetrate the vortices, even after several minutes (many vortex turnover times).

For eastward (co-rotating) jets, a narrow wavy jet was found to exist up to the highest accessible forcing. Dye injected into the jet diffused quickly within the jet, and then slowly filled the region outside of the jet (and, to

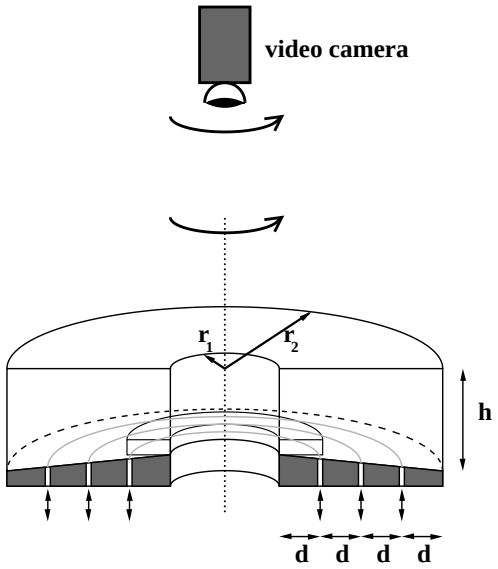

Fig. 1. Schematic of rotating annulus: $r_1 = 10.8$ cm, $r_2 = 43.2$ cm, $d = 8.1$ cm, and $h = 20.3$ cm at r_2. See text for details. The configuration of the annulus was slightly different for the experiments described in section 2 [6], [7], [8].

a lesser extent, inside) through a series of tongues generated from the crests of the traveling wave [6], [8]. Dye injected far from the jet spread uniformly in the region delimited by the jet, but virtually no cross-jet transport was observed, even after 500 rotations of the annulus. This effective dynamical barrier appears to work in much the same way the southern polar night jet acts as a barrier to transport of ozone from lower latitudes into the polar region.

3 Trajectories in vortex chains

For less energetic flows, we have performed detailed measurements of individual particle trajectories in single annular chains of vortices to investigate the role of chaotic advection in particle transport [9-12]. These experiments were performed at Reynolds numbers above the initial instabilities in the axisymmetric flow that exists at very low forcing, but below any indications of turbulent flow. At low pumping rates, the vortex chain rotates at a constant rate, producing a periodic signal on a hot film velocity probe mounted at a fixed position on the annulus (Fig. 2(a)).

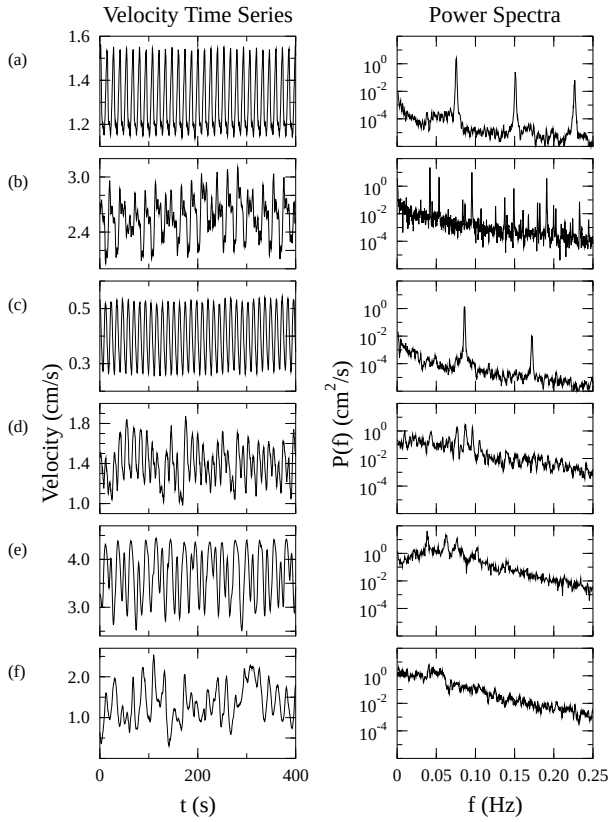

Fig. 2. Velocity time series and power spectral density $P(f)$ obtained from hot film probe measurements of the azimuthal velocity component at $r = 35.1$ cm: (a) *time-independent flow*; (b) *seven-vortex flow* with periodic time dependence in the reference frame co-rotating with the vortex chain (see Fig. 3); (c) *six-vortex flow* with periodic time dependence in the vortex chain reference frame; (d) *five-vortex flow* with chaotic time dependence; (e) *four-vortex flow* with chaotic time dependence (see Fig. 4); (f) *weakly turbulent flow* (see Fig. 5). These data are taken in the *tank* frame of reference, as opposed to the co-moving frame of reference used for the particle pictures in this paper.

Transport is measured by putting several hundred small (~ 1 mm diameter), neutrally buoyant tracer particles into the tank. They are illuminated by light shining through the outer cylinder of the annulus and are viewed through a video camera rotating above the experimental set up. Automated tracking techniques [13] are used to find the trajectories of the individual particles.

3.1 Flows Studied

At the forcing rates used in this experiment, a counter-rotating jet is unstable to a chain of four, five, six, or seven vortices above the outer ring of holes [14]. The instability at the inner shear layer is inhibited by a 6.0 cm tall annular Plexiglas barrier with outer radius of 19.4 cm that is inserted above the inner ring of holes (see Fig. 1). (Without the barrier, the flow would be composed of two vortex chains, one above each forcing ring [14].) The vortex chain rotates relative to the tank at approximately half the speed of the azimuthal jet as seen in the annulus frame of reference (typically 4 cm/s). In a reference frame moving with the vortices, the vortex chain is sandwiched by azimuthal jets going in opposite directions (e.g. Fig. 3).

We study transport in flows generated with six different forcing techniques, using either water (kinematic viscosity $\nu = 0.009$ cm^2/s), or a water-glycerol mixture (38% glycerol by weight; a kinematic viscosity $\nu = 0.03$ cm^2/s). The time-dependence of some of the flows are similar, so in this paper we label some of the flows by their structure (number of vortices). The six flows, listed with the pumping rate, F, tank rotation rate, $\Omega/2\pi$, and working fluid, are:

1. *Time-independent flow* with six vortices ($F = 45$ cm^3/s, $\Omega/2\pi = 1.5$ Hz, water-glycerol). The inner (outer) ring of holes acts as a source (sink) through which fluid is pumped into (from) the tank. In the reference frame co-rotating with the vortex chain, the flow is time-independent (Fig. 2(a)). This flow should not have chaotic mixing; tracers should follow closed streamlines.
2. *Seven-vortex flow* with quasi-periodic time dependence (see Fig. 3; $F = 45$ cm^3/s, $\Omega/2\pi = 1.5$ Hz, water-glycerol). The parameters for this flow are the same as the time-independent flow, but the initial conditions were different. In the reference frame co-rotating with the vortex chain, this flow is time-periodic; in the reference frame of the tank, the motion of the vortices around the annulus results in quasi-periodic time dependence (Fig. 2(b)). This flow is termed "modulated wave flow" in Ref. [11].
3. *Six-vortex flow* with quasi-periodic time dependence ($F = 45$ cm^3/s, $\Omega/2\pi = 1.5$ Hz, water-glycerol). This flow is generated with the same techniques as the time-independent flow, except that the radial forcing has a non-axisymmetric perturbation. The forcing flow through one 60° sector of source and sink holes is restricted to less than half that for the rest of the forcing holes. Thus the vortex chain is perturbed as it moves past this constricted sector, with the period of the perturbation being the time for a vortex to precess around the annulus (70.0 s). In the reference frame of the vortex chain, the flow is time-periodic. In the reference frame of the tank, the flow is also time-periodic (Fig. 2(c)), as the perturbation is stationary with respect to the tank. In all other reference frames, the flow is quasi-periodic in time. This flow is termed "time-periodic flow" in Refs. [10], [11].

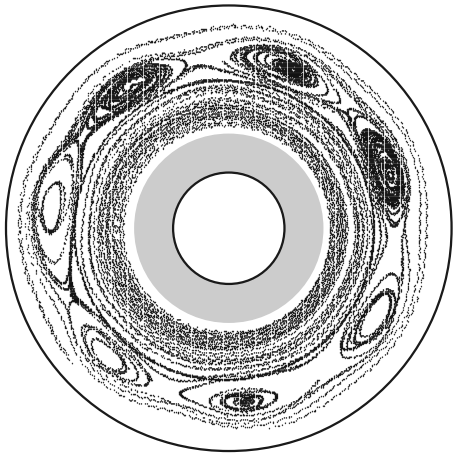

Fig. 3. The *seven-vortex flow* is revealed by the trajectories of 20 particles tracked for 300 s in a reference frame co-rotating with the vortices. In this reference frame, the vortex chain is sandwiched between two azimuthal jets. This flow has periodic time dependence in this reference frame. The inner and outer circles represent the annulus boundaries, and the grey circle indicates the location of the Plexiglas barrier. (Figure from Ref. [11].)

4. *Five-vortex flow* with chaotic time dependence ($F = 45$ cm^3/s, $\Omega/2\pi = 1.5$ Hz, water-glycerol). This flow is similar to the six-vortex flow, except that the flux through the perturbing sector is completely shut off. There are still well-defined vortices in this flow, but the number of vortices alternates between five and six over long periods of time. This flow has chaotic time-dependence, as can be seen from the hot film probe measurements (Fig. 2(d)). The word chaotic in this case denotes Eulerian chaos, that is, a chaotic velocity field, as distinct from Lagrangian chaos of the particle trajectories. This flow is termed "chaotic flow" in Refs. [10], [11]. We do not actually know this flow is chaotic in the sense of positive lyapunov exponents, but the noise floor shown in Fig. 2(d) is higher than the previous flows, a signature of chaos.
5. *Four-vortex flow* with chaotic time dependence (see Fig. 4; $F = 52$ cm^3/s, $\Omega/2\pi = 1.0$ Hz, water). Rather than the inner and outer forcing rings, this flow uses the inner and middle forcing rings ($r = 18.9$ cm and 27.0 cm), to allow the vortices to be larger, and prevent an inner jet from forming, as can be seen in Fig. 4.

   At this high pumping rate, the motion of the vortices is chaotic, as shown in the velocity power spectrum shown in Fig. 2(e). As with the five-vortex flow, this is Eulerian chaos. This flow was termed "chaotic flow" in Ref. [12]. (Again, the chaos of this flow has not been rigorously

Fig. 4. The *four-vortex flow* is revealed by the trajectories of 12 particles tracked for 100 s in a reference frame co-rotating with the vortices. The inner and outer circles represent the annulus boundaries, and the grey circle indicates the location of the Plexiglas barrier. (Figure from Ref. [12].)

confirmed, but the power spectrum is reasonable evidence of the chaos of the flow, as are the qualitative observations of the vortex motion.)

6. *Weakly turbulent flow* (see Fig. 5; $F = 45$ cm^3/s, $\Omega/2\pi = 1.5$ Hz, water). This flow was generated using a special forcing configuration. Only the outer ring of holes was used ($r = 35.1$ cm). The ring is divided into 60° sectors, alternating between sources and sinks. The resulting flow consists of vortices of both signs, and there are no persistent jets or other structures. Note that the previous flows are all laminar; this is the only velocity field that is turbulent.
   The velocity power spectrum consists of broadband noise and no dominant spectral components; see Fig. 2(f). This flow is termed "turbulent flow" in Ref. [10] and "weakly turbulent flow" in Ref. [11].

The flows are summarized in Table 1.

3.2 Analysis techniques

After a typical experimental run of 4 hours, we have tracked typically 5-10 trajectories with duration greater than 20 minutes, 30 with 10-20 minutes duration, and several hundred with 2-10 minutes duration. Statistics for the longer times are improved by repeating the experiments with the same control parameters (but see discussion in Sec. 5).

The transport is analyzed as a one-dimensional process in the azimuthal direction θ. The variance is calculated by the relations

Fig. 5. Two trajectories show the lack of long-lived coherent structures in the *weakly turbulent flow*. The beginning and end of one trajectory is marked with circles, the other with squares; both particles start at the far right. The inner and outer circles represent the annulus boundaries, and the grey circle indicates the location of the Plexiglas barrier. The particles are shown in the reference frame of the annulus. (Figure based on Ref. [11].)

Table 1. Summary of the flows investigated, with kinematic viscosity ν, pump flux F, and dimensionless numbers Ro, Ek, and Re (calculated using $U = 3$ cm/s as the typical velocity for all flows). The rotation rate $\Omega/2\pi = 1.5$ Hz for all flows (except the four-vortex flow, where $\Omega/2\pi = 1.0$ Hz). Time dependence listed is in the reference frame co-rotating with the vortex chain. The pumping configuration for each flow are described in Sec. 3.1.

Flow name	ν (cm^2/s)	F (cm^3/s)	$Ro \times 10^2$	$Ek \times 10^6$	Re
Time-independent (with six vortices)	0.03	45	4.0	4.0	400
Seven-vortex (time-periodic)	0.03	45	4.0	4.0	400
Six-vortex (time-periodic)	0.03	45	4.0	4.0	400
Five-vortex (Eulerian chaos)	0.03	45	4.0	4.0	400
Four-vortex (Eulerian chaos)	0.009	52	12	2.0	1000
Weakly turbulent	0.009	45	16	1.2	1100

$$\sigma^2(t) = \langle \Delta\theta^2(t,\tau)\rangle - \langle \Delta\theta(t,\tau)\rangle^2 \quad , \tag{1}$$
$$\Delta\theta(t,\tau) = \theta(\tau+t) - \theta(\tau) \quad ,$$

where the ensemble average is over τ for individual trajectories and over the different trajectories in the run. This procedure treats each tracer as though starting from the same angle at the same time. Only those trajectories that display both sticking and flight events are used in the calculation of the variance. The first and last events (sticking or flight) are removed to avoid any biasing. (That is, when a particle is first observed, it is in the middle of an event; we consider the trajectory only after this event has finished, so that all particles are considered at the beginning of a flight or sticking event, rather than in the middle of an event.) Different analysis techniques were examined to insure that the results are not strongly dependent on the biasing effects.

Sticking and flight time probability distribution functions (PDFs) are determined from local extrema of $\theta(t)$; see, e.g., Fig. 8. A flight is identified by an angular deviation $\Delta\theta > \Theta_{\rm vortex}$ (angular width of a single vortex) between successive extrema, and the sticking events are the intervals between flights. The PDFs are normalized histograms of the durations of these events. Histograms are generated with logarithmic binning, normalized, and plotted on log-log or log-linear scales.

The exponents derived from the PDFs are corrected to account for biases toward shorter sticking/flight times that arise from the finite duration of the measured trajectories. The adjustment is determined by generating long, artificial trajectories numerically with known, ideal power law sticking and flight time distributions. These long trajectories are then chopped randomly into smaller sections with a distribution of durations comparable to those in the experiment. PDFs determined from these chopped trajectories are also biased toward smaller times. The adjustment is determined by comparing the PDFs from the chopped trajectories to the ideal PDFs (both from numerical data); the exponents characterizing the PDFs for the chopped time series are about 0.3 larger than for the original long time series. Note that all reported exponents (e.g. Table 2) are the *corrected* values; the values measured directly from the PDFs are reported in the captions for each PDF figure.

4 Results

4.1 Time-independent flow: no chaotic mixing

Ideally, particle trajectories in a time-independent flow fall on closed streamlines and there is no chaotic advection. While molecular diffusion of the tracer particles is completely negligible on the time scale of the experiments, slight imperfections due to noise, Ekman pumping, and finite-size particle effects can have a noticeable effect on the trajectories. Such imperfections are inevitable in an experiment, even when Fourier spectra indicate that the velocity field is time-independent, as is the case for the flow in Fig. 6. The imper-

fections allow tracers to wander between neighboring streamlines, apparently filling the interior of a vortex; see Fig. 6(a). The imperfections occasionally lead to the escape of a tracer particle near a separatrix, but we find that in practice tracers remain trapped for long periods of time. Trapping times of 800 s (approximately 40 vortex turnover times) such as the one shown in Fig. 6(a) are common. Similarly, tracers that start in a jet remain in the jet for long times, e.g. Fig. 6(b).

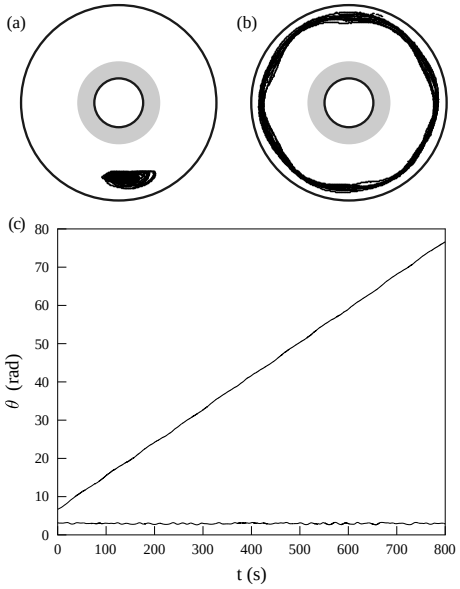

Fig. 6. (a) and (b) Tracer particle trajectories in the time-independent flow, viewed in a reference frame co-rotating with the vortex chain. (c) The azimuthal displacement as a function of time for the particles in (a) and (b); the starting angle $\theta(t = 0)$ is arbitrary. The inner and outer circles represent the annulus boundaries, and the grey circle denotes the Plexiglas barrier. (Figure based on Ref. [10].)

The azimuthal coordinate $\theta(t)$ for a particle in a vortex oscillates about a constant value, while for a particle in a jet with constant velocity, $\theta(t)$ grows linearly with time, as shown in Fig. 6(c). In the absence of noise, the variance of a distribution of particles grows as t^2 (ballistic separation) [15].

4.2 Time-periodic flows: power law flights

Chaotic advection is observed in the seven- and six-vortex flows, the two flows that have periodic time dependence in the reference frame co-rotating with

the vortex chain. Particles frequently make transitions to and from vortices, as seen in Fig. 7. Instead of being trapped indefinitely, particles have sticking events interspersed with flights in the jet regions.

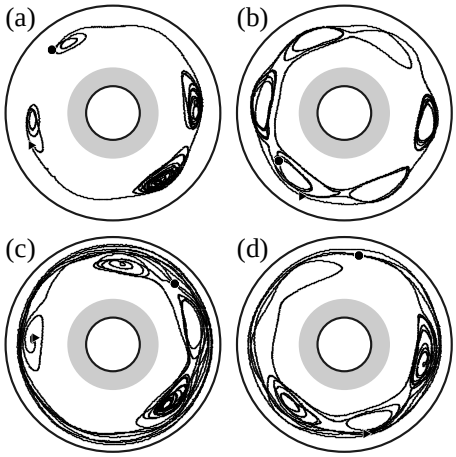

Fig. 7. Chaotic particle trajectories in the six-vortex flow (time-periodic in the reference frame of the vortex chain). Long sticking events can be seen in each case, and flights of length greater than one rotation about the annulus can be seen in (c), (d). Hyperbolic fixed points, near which the particle motion is particularly susceptible to transitions between flights and sticking events, are evident in all of the trajectories. The particle motion is viewed from a reference frame that is co-rotating with the vortex chain, and the beginning of each trajectory is marked by a triangle, the end by a circle. (Note that this is incorrectly labeled in Ref. [10], as can be seen by comparing Fig. 6(a) and Fig. 7(a) in that article. It is also incorrectly labeled in Ref. [9]; compare Fig. 1(b) and Fig. 2(b).) These trajectories are from the six-vortex flow, but are typical in appearance for the seven-vortex and five-vortex flows. (Figure based on Ref. [10].)

This intermittent sticking/flight behavior is apparent in plots of $\theta(t)$, as shown in Fig. 8. The observed sticking times and flight times range from $\sim$10 s to $\sim$600 s. The lower boundary of $\sim$10 s is half a vortex turnover time. (The vortex turnover time, measured by doubling the average time between successive reversals for particles in a vortex, is $\sim$23 s. The five-vortex and six-vortex flows have similar vortex turnover times, $\sim$20 s.)

In Fig. 8 it can be seen that the slopes of the flight segments are approximately constant, indicating that the azimuthal velocity, $\omega = d\theta/dt$, remains steady during the flights, except when the tracer passes near a hyperbolic point, where both ω and the radial component of velocity can decrease nearly to zero. Some asymmetry is observed in the flight speed and the relative prob-

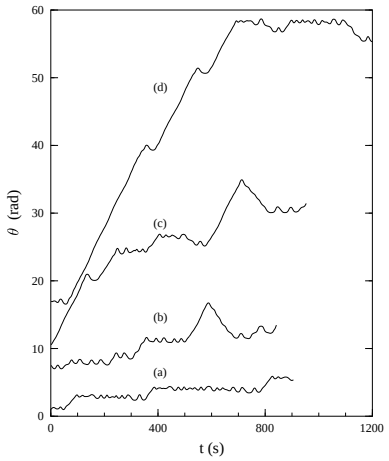

Fig. 8. Azimuthal displacement $\theta(t)$ as a function of time for the particle trajectories in Fig. 7. The oscillations of the tracer particle trajectories correspond to motion around a vortex, and the diagonal lines correspond to flights. The starting angle $\theta(t = 0)$ is arbitrary. These trajectories are from the six-vortex flow, but are typical in appearance for the seven-vortex and five-vortex flows. (Figure from Ref. [10].)

ability of clockwise and counter-clockwise flights, but the PDF exponents appear to be the same. A numerical simulation designed to approximate these flows showed significant asymmetry [16].

To find the PDFs for the flight and sticking events, the trajectories of 1300 particles were analyzed for the seven-vortex flow, and 1700 particles for the six-vortex flow. The cleanest data (of all six flows) were obtained for the quasi-periodic seven-vortex flow, and the results are shown in Fig. 9. The flight PDF shows clear power law decay, $P_F(t) \sim t^{-\mu}$ with $\mu = 3.2 \pm 0.2$. The PDFs for flights in the $+\theta$ and $-\theta$ directions were compared and found to have similar decay exponents. The sticking PDF has a curvature indicating asymptotic behavior steeper than a power law (but does not appear exponential).

The fact that the velocity of the flights are approximately constant, and that the PDF show power law behavior suggests that the results of of the continuous time random walk model (CTRW) developed in Refs. [12], [17], [18] are applicable to this system. The results relevant for this work are summarized in figure 10, which shows the predicted variance exponent γ as a function of the exponents μ and ν of the flight and sticking PDFs, for both symmetric and asymmetric random walks. For a detailed discussion of the model, see Ref. [12].

Since $\mu > 3$ for this flow, the Central Limit Theorem predicts normal diffusion ($\sigma^2(t) \sim t^\gamma$ with $\gamma = 1$). We compute the variance as discussed in

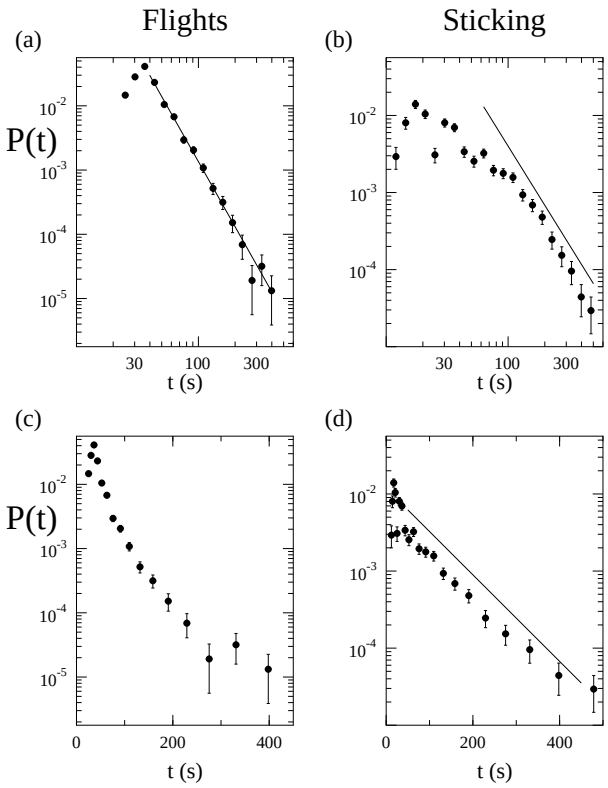

Fig. 9. Seven-vortex flow: (a,c) flight and (b,d) sticking probability distribution functions, shown on (a,b) log-log axes and (c,d) log-linear axes. The error bars show the statistical uncertainty ($\sqrt{N}$). The flight PDF shows power law decay, $P_F \sim t^{-\mu}$; the line drawn in (a) is a least squares fit to the decaying data yielding $\mu = 3.2 \pm 0.2$. The sticking PDF does not show a clear power law decay nor an exponential decay; the straight line (drawn for comparison) in (b) has a slope of -2.55, with the slope obtained from a least squares fit to the last 8 points in the tail. (The uncorrected value of μ is 3.4 ± 0.2; see Sec. 3.2 for details of the correction.)

Sec. 3.2, with the results shown in Fig. 11. The slope of the variance plot is shown in the inset, and suggests that the variance grows superdiffusively. For short times ($t < 10$ s), the variance grows ballistically, $\gamma = 2$. This is because of the vortex turnover time: for times less than ∼10 s, particles in flight are indistinguishable from those stuck in a vortex [19]. Particles all appear to be moving with a constant velocity (different for each particle), some in opposite directions, and thus the variance must grow ballistically.

For longer times, γ cannot be determined accurately, most likely due to a lack of trajectories with long durations. It is clear that for our data γ does not ever approach 1, the value expected for normal diffusion. The Berry-

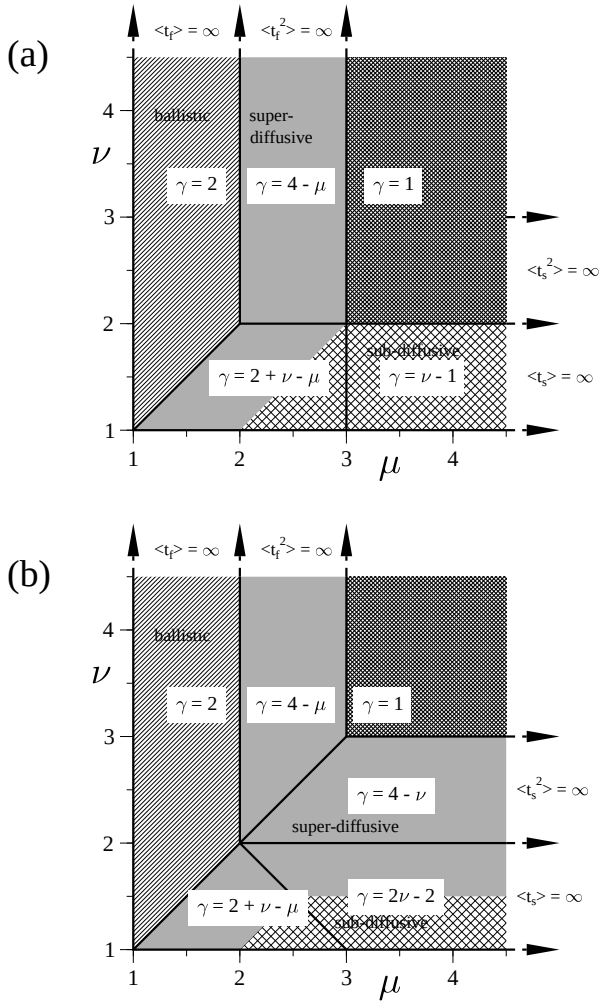

Fig. 10. Phase diagrams for variance of (a) symmetric and (b) asymmetric (or biased) random walks, from Ref. [12]. μ and ν are the exponents controlling the asymptotic power law decay of the flight and sticking PDFs, respectively: $P_F(t_\mathrm{f}) \sim t_\mathrm{f}^{-\mu}$ and $P_S(t_\mathrm{s}) \sim t_\mathrm{s}^{-\nu}$, as $t \to \infty$. For each region, bordered by the solid lines, the relationship between the variance exponent γ [$\sigma^2(t) \sim t^\gamma$] and μ and ν is shown. The shadings indicate areas where the behavior is normally diffusive ($\gamma = 1$), subdiffusive ($\gamma < 1$), superdiffusive ($\gamma > 1$), and ballistic ($\gamma = 2$).

Esséen theorem predicts that the time for a (symmetric) random walk to reach normally diffusive behavior scales as [20], [21]

$$t \sim \left(\frac{\langle |l|^3 \rangle}{\langle l^2 \rangle^{3/2}} \right)^2 \quad , \tag{2}$$

where the moments are for the flight length PDF. For the seven-vortex flow, however, the third moment is infinite, since $\mu < 4$. From Ref. [12], the first two exponents in an asymptotic expansion for the variance at long time, $\sigma^2(t) \sim Ct^\gamma + C't^{\gamma'}$ are $\gamma = 1$ and $\gamma' = 0$ for $\mu > 4$, so that only the leading term grows with time. For $3 < \mu < 4$, however, $\gamma = 1$ and $\gamma' = 4 - \mu$, thus the second order term also grows with time, and a very slow convergence is expected.

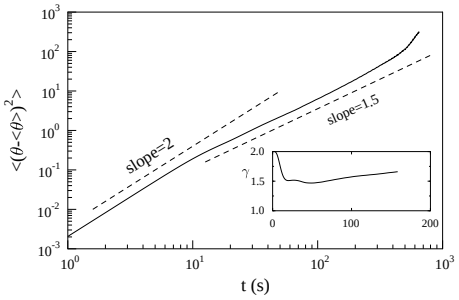

Fig. 11. Variance $\sigma^2(t)$ for the ensemble of tracer particles for the seven-vortex flow (solid line). The slope, shown in the inset, indicates that the variance grows superdiffusively. (Figure based on Ref. [11].)

The flight and sticking PDFs for the six-vortex flow are shown in Fig. 12. Again, the flight PDF shows clear power law decay, with a slope of $\mu = 2.5 \pm 0.2$. The PDFs for leftward and rightward flights separately had similar decay exponents (within their uncertainties). The sticking PDF clearly decays faster than a power law, although it is unclear if the decay is exponential. Note that this interpretation is different from Refs. [9], [10], where it is stated that the sticking-time PDF appears to show power law decay. (The PDFs in those articles were constructed with constant-width bins, so the deviation from power law behavior was less evident.)

Again, the results can be compared with the analysis from the CTRW. The six-vortex flow particles are undergoing an asymmetric random walk with $\mu = 2.5$ and $\nu \to \infty$, suggesting that the variance should grow as $\sigma^2(t) \sim t^\gamma$ with $\gamma = 4 - \mu = 1.5$, that is, superdiffusively (see Fig. 10(b)). Figure 13 shows that for $t > 20$ s, the variance grows with $\gamma = 1.65 \pm 0.15$. Given the uncertainty of μ (± 0.2), the predicted and measured values for γ

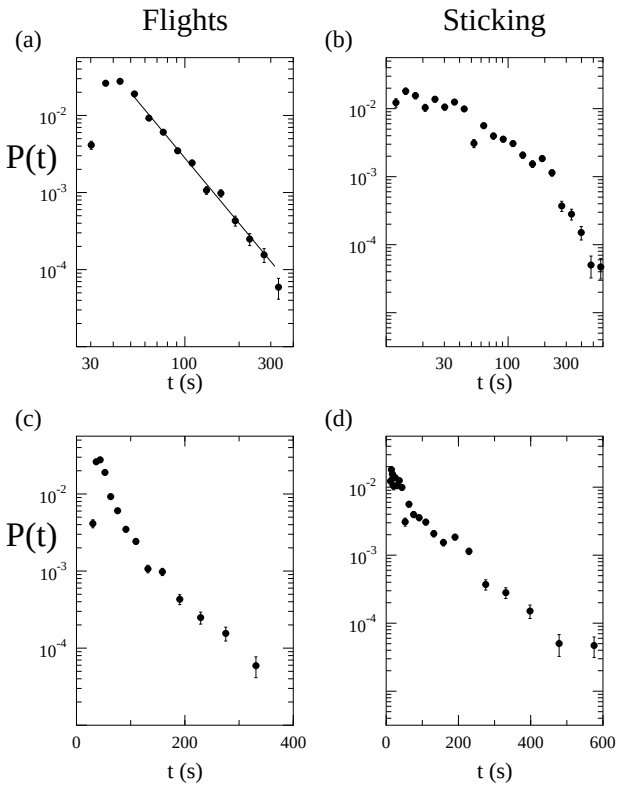

Fig. 12. Six-vortex flow: (a,c) flight and (b,d) sticking probability distribution functions, shown on (a,b) log-log axes and (c,d) log-linear axes. The error bars show the statistical uncertainty ($\sqrt{N}$). The flight PDF shows power law decay, $P_F \sim t^{-\mu}$; the line drawn in (a) is a least squares fit to the decaying data yielding $\mu = 2.5 \pm 0.2$. The sticking PDF does not show a clear power law decay nor an exponential decay. Note that these PDFs are slightly different from those shown in Refs. [9], [10] due to the improvement in binning technique (Sec. 3.2). (The uncorrected value of μ is 2.8 ± 0.2; see Sec. 3.2 for details of the correction.)

are in accord. As noted above for the seven-vortex flow, the variance grows ballistically for times shorter than a vortex turnover time.

While both the seven-vortex flow and the six-vortex flow have periodic time dependence, it is not surprising that the transport results are different. The seven-vortex flow has naturally arising time-dependence, while the six-vortex flow is perturbed periodically by an artificial change in the forcing (as described in Section 3.1). In the vortex reference frame, the instability of the seven-vortex flow has a frequency of 0.00033 Hz and a mode number of 3 (measured from particle tracking). The mechanical perturbation of the

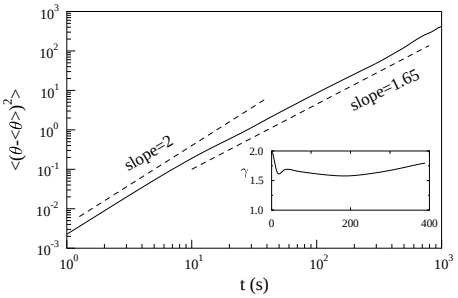

Fig. 13. Variance $\sigma^2(t)$ for the ensemble of tracer particles for the six-vortex flow (solid line). The slope, shown in the inset, indicates that the variance grows superdiffusively, with $\gamma = 1.65 \pm 0.15$. (Figure based on Ref. [9].)

six-vortex flow appears with a frequency of 0.014 Hz (in the vortex reference frame) and is mode number 1.

4.3 Chaotic flows

The two chaotic flows, the five-vortex flow and the four-vortex flow, also exhibited chaotic mixing. As with the seven- and six-vortex flows, the difference between the two chaotic flows is the nature of the forcing: the chaotic time dependence of the five-vortex flow is due to the mechanical perturbation, while the chaotic time dependence of the four-vortex flow arises from natural instabilities.

The trajectories for the five-vortex flow appear similar to those shown in Fig. 7, while typical trajectories of the four-vortex flow are shown in Fig. 14. The four vortices are not stationary but move erratically. (The pictures shown are taken in a frame of reference co-rotating with the *average* speed of the vortex chain, but there is substantial variation in the *instantaneous* speed of each vortex.)

Figure 15 shows the angular position of the particles as a function of time in the four-vortex flow. The oscillatory behaviors correspond to motion when the particle is "sticking" in a vortex, and the longer diagonal lines are flights in the outer jet. Flights are distinguished from sticking motions by examining the azimuthal distance traveled before reversing direction: particles travel in a vortex for at most $\pi/2$ radians before changing directions, while a particle that leaves one vortex and enters the next (the minimum flight distance) will move at least $\pi/2$ radians. Unlike the other flows, for the four-vortex flow there is no strong inner jet and particles do not travel long distances on the inner side of the vortex chain. Approximately 10% of the flights seen in the four-vortex flow are short hops on the inner side of the vortex chain, from

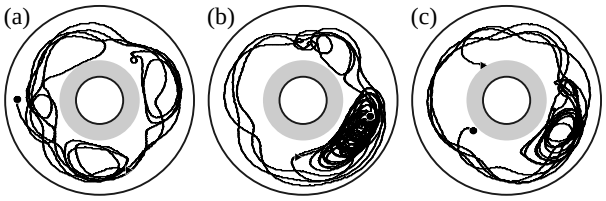

Fig. 14. Chaotic particle trajectories in the four-vortex flow (chaotic time dependence). Nearly all of the flight behavior is in the outer jet; a brief flight in the inside can be seen in (a). The chaotic motion of the four vortices can be seen in (b), where the particle spends most of its time in the same vortex which moves erratically. The beginning of each trajectory is marked by a circle, the end by a triangle. (Figure from Ref. [12].)

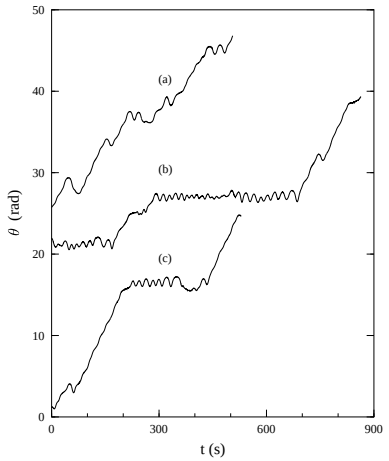

Fig. 15. Angular displacement $\theta(t)$ as a function of time for the trajectories shown in Fig. 14. Diagonal lines indicate flights, while the small oscillations correspond to particle motion within a vortex. Despite the chaotic motion of the vortices, a clear distinction can be made between flight behavior and sticking behavior. (Figure from Ref. [12].)

one vortex to an adjacent vortex; these hops take less than 40 s, and do not contribute to the long-time statistics.

To compile the flight and sticking PDFs, 1100 particles were examined for the five-vortex flow and 210 particles were examined for the four-vortex flow. (It was very difficult to track particles for long times for the four-vortex flow; particles disappeared from the visible area rapidly.)

The flight and sticking PDFs for the five-vortex flow are shown in Fig. 16. Neither PDF shows power law decay, nor do they show convincing exponential decay. Note that this interpretation is different from that given in Ref. [10].

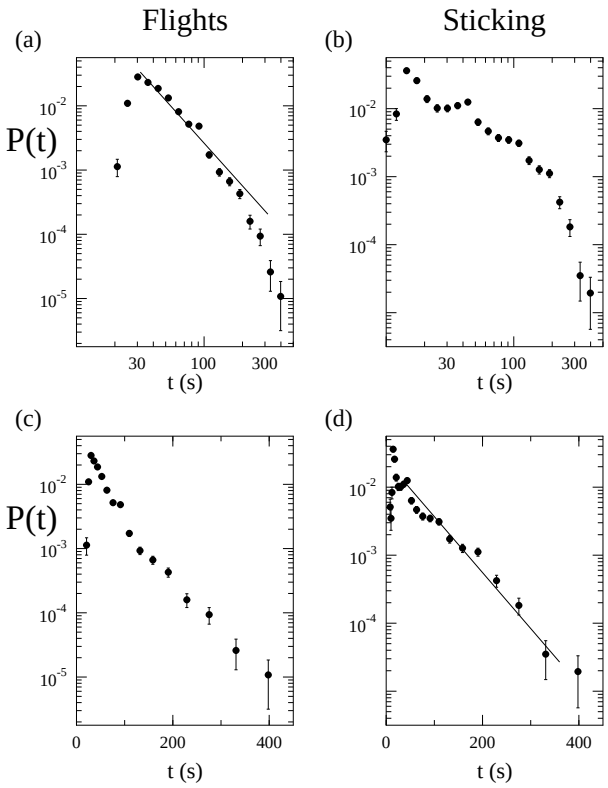

Fig. 16. (a,c) flight and (b,d) sticking probability distribution functions, shown on (a,b) log-log axes and (c,d) log-linear axes, for the five-vortex flow. The error bars show the statistical uncertainty ($\sqrt{N}$). The flight PDF appears to decay faster than a power law; the line drawn for comparison has a slope of -2.2, and is a least squares fit to the data for $t > 30$ s. The sticking PDF does not show a clear power law decay nor an exponential decay, although the data in (d) look roughly linear; a least squares fit line is shown. Note that these PDFs are slightly different from those shown in Ref. [10] due to the improvement in binning technique (Sec. 3.2). (Figure based on Ref. [10].)

As discussed in Sec. 4.2, this is presumably due to an improvement in the analysis technique.

Given the uncertainty of the decay rate of the flight and sticking PDFs, comparison with the results of the CTRW model is difficult. The most reasonable interpretation of Fig. 16 would be $\mu \to \infty$, $\nu \to \infty$, yielding $\gamma = 1$ by the Central Limit Theorem. The growth of the variance measured from the experiment is shown in Fig. 17, and shows superdiffusive growth with $\gamma = 1.55 \pm 0.15$.

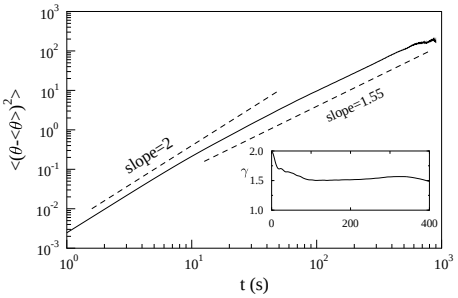

Fig. 17. Variance $\sigma^2(t)$ for the ensemble of tracer particles for the five-vortex flow (solid line). The slope, shown in the inset, indicates that the variance grows superdiffusively with $\gamma = 1.55 \pm 0.15$. (Figure based on Ref. [10].)

The PDFs for the four-vortex flow are shown in Fig. 18. This is the only flow for which both flight and sticking PDFs show power law decay. The decay exponents, adjusted for finite trajectory duration, are $\mu = 2.0 \pm 0.2$ (flight) and $\nu = 1.3 \pm 0.2$ (sticking). (This implies an infinite mean residence time for particles in a vortex, which would violate the incompressibility condition [22]. The PDF presumably falls off at longer times not accessible experimentally.) It is remarkable that these PDFs have a power law form despite the presence of Eulerian chaos. Although the vortices are moving erratically with respect to each other, particle motion still displays the effects of long-time correlations. The model of Refs. [22], [23] exhibits power law flight PDFs for chaotic vortex motion because the outer boundary of the annulus plays the role of an invariant surface.

The behavior of the variance at long times for the four-vortex flow can be analyzed with the CTRW. Taking $\nu = 1.3$ and $\mu = 2.0$, the variance should grow as t^γ with $\gamma = 2 + \nu - \mu \approx 1.3$. The experimentally determined variance for this flow is shown in Fig. 19. It is difficult to track particles for long enough times in this flow to gather the statistics necessary to determine the variance accurately; hence quantitative comparison with the results of the CTRW is difficult. However, the behavior appears superdiffusive with an exponent γ between 1.5 and 2.0. At longer times, the exponent drops below 1.5, and the prediction is in the limit $t \to \infty$, so the experimental results appear consistent with the calculation.

The failure of the variance to reach its asymptotic behavior despite the large number of long time trajectories can be understood from an analysis of crossover times in the CTRW model. The time necessary to approach the asymptotic state can be calculated by retaining lower order terms in the expansion for σ (see Ref. [12] for details). Using the values of $\mu = 1.9, \nu = 1.3$, and cutoff times $t_F = 22$ s, $t_S = 10$ s, yields $\sigma \sim 0.055 t^{1.4} - 0.10 t^{1.1}$. A plot of this function on a log-log scale does not reach a slope of 1.5 until 400 s,

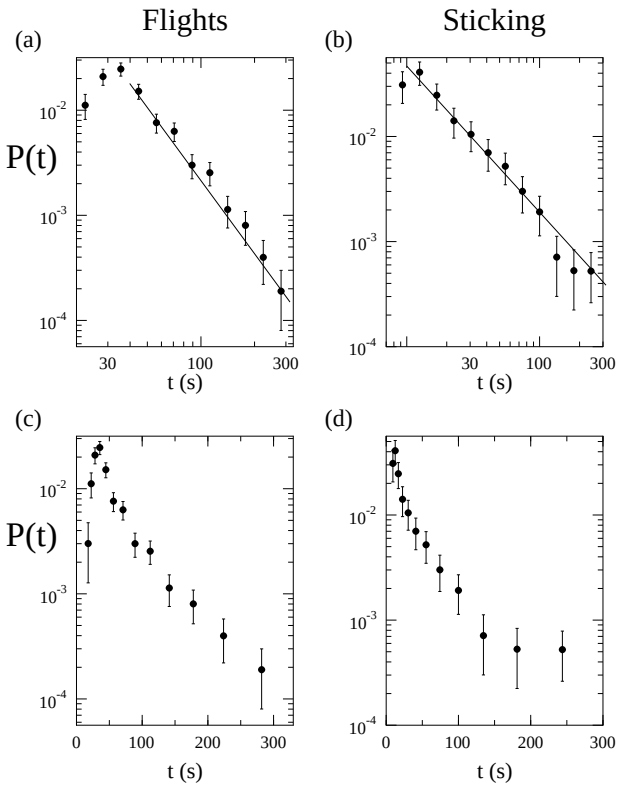

Fig. 18. Four-vortex flow: (a,c) flight and (b,d) sticking probability distribution functions, shown on (a,b) log-log axes and (c,d) log-linear axes. The error bars show the statistical uncertainty ($\sqrt{N}$). The flight PDF decays as a power law, $P_F(t) \sim t^{-\mu}$, with $\mu = 2.0 \pm 0.2$. The sticking PDF also appears to decay as a power law, with a decay exponent of $\nu = 1.3 \pm 0.2$. The error bars for these PDFs are much larger than for Figs. 9, 12, and 16 as this flow had much less data. (The uncorrected value of μ is 2.3 ± 0.2, ν is 1.4 ± 0.2; see Sec. 3.2 for details of the correction.)

and our data only extend to ∼500 s. This slow convergence to asymptotic behavior is a generic feature of Lévy processes and complicates analysis in many experimental situations and numerical simulations (see discussion in Sec. 5).

Figure 20 shows that the mean particle position $\langle x \rangle$ for the four-vortex flow grows approximately linearly with time for most of the range. For longer times, $\langle x \rangle$ appears to start growing faster than linearly in time. For times less than a vortex turnover time, linear growth is expected, as all particles are moving with constant velocity (whether in a vortex or in the jet). For longer times, the model of Ref. [12] predicts (for $\mu = 2.0$ and $\nu = 1.3$) that

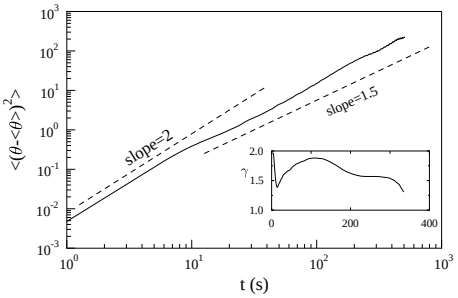

Fig. 19. Variance $\sigma^2(t)$ for the ensemble of tracer particles for the four-vortex flow (solid line). The slope, shown in the inset, indicates that the variance grows superdiffusively. (Figure based on Ref. [12].)

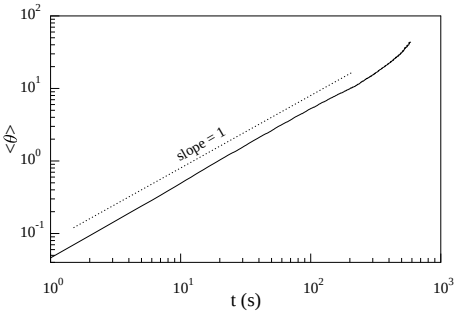

Fig. 20. Mean particle position for four-vortex flow, $\langle\theta(t)\rangle$ (solid line). (Figure from Ref. [12].)

$\langle x\rangle \sim t^{0.3}$. It is probable that the asymptotic scaling is not reached due to lack of statistics at long times (see [12]).

4.4 Weakly turbulent flow: no long flights

The absence of long-lived vortices and azimuthal jets leads to a behavior in the turbulent regime that contrasts markedly with that in the laminar and chaotic regimes. Tracers in the turbulent flow wander erratically, and there are no well-defined flights (which are dependent on jet regions) or sticking events: compare plots of trajectories in the turbulent flow, Fig. 5, with those for the six- and four-vortex flows, Figs. 7 and 14, and compare plots of azimuthal displacement $\theta(t)$ in Fig. 21 with Figs. 8 and 15.

While there are no flights or sticking events in the turbulent flow, the trajectories can be treated as random walks by defining a step as the time between two successive extrema in $\theta(t)$. We find that the probability distribution function is exponential, $P(t) \propto e^{-t/\tau}$, with $\tau = 15.2$ s (see Fig. 22),

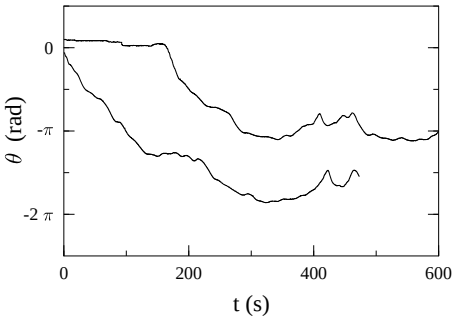

Fig. 21. Angular displacement $\theta(t)$ as a function of time for the trajectories shown in Fig. 5. The upper trace is for the particle marked with circles. (Figure from Ref. [11].)

in contrast to the power law PDFs observed for flights in the time-periodic and chaotic regimes.

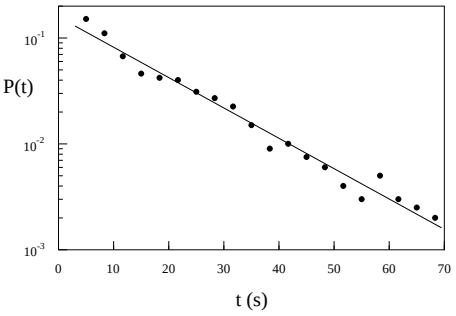

Fig. 22. Probability distribution for azimuthal displacement in the turbulent flow. The distribution is exponential with a decay time of 15.2 s. (Figure from Ref. [10].)

The slope γ of a log-log plot of the variance $\sigma^2(t)$ (Fig. 23) drops steadily from 2 and appears to approach the value expected for normal diffusion ($\gamma = 1$) at long times; however, we cannot follow particles for long enough times to unambiguously determine the asymptotic behavior. This result is consistent with the Central Limit Theorem, which predicts $\gamma = 1$ for an exponentially decaying flight PDF. This also agrees with a result derived in 1921 by Taylor [19]. Taylor showed that for very short time scales, a turbulent flow should have ballistic mixing ($\sigma^2(t) \sim t^2$). This ballistic behavior lasts until particle motions become uncorrelated; for our weakly turbulent flow, this time scale appears to be about 6 s.

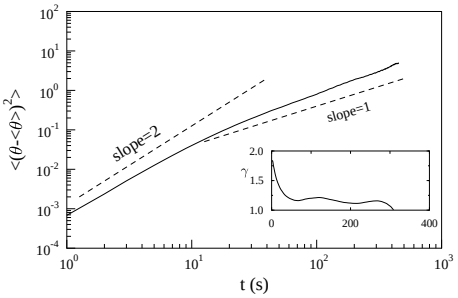

Fig. 23. Variance $\sigma^2(t)$ for the ensemble of tracer particles for the weakly turbulent flow (solid line). The slope, shown in the inset, suggests the long term behavior may be normally diffusive. (Figure based on Ref. [10].)

A diffusion coefficient can be found for the turbulent flow by fitting the variance data, yielding $D = 0.010 \pm 0.003\,\mathrm{rad}^2/\mathrm{s}$. The data was fit for $t > 10$ s and for $t > 100$ s, both giving a similar value. By using $r = 30$ cm as the approximate radial position of the particles, the diffusion coefficient can be written as $D_{\mathrm{eff}} = 9\ \mathrm{cm}^2/\mathrm{s}$. For particles diffusing purely due to Brownian motion, the Einstein relation for the diffusion coefficient is $D_{\mathrm{Brownian}} = RT/6\pi\eta a N$ with R the universal gas constant, η the dynamic viscosity, a the particle radius, and N Avagadro's number [24]. For our tracer particles this formula yields $D = 4.4 \times 10^{-12}$, a factor of 10^{12} smaller that the measured diffusion coefficient.

5 Discussion

We have found superdiffusion in a variety of flows. The data from the six regimes are summarized in Table 2. Except for the five-vortex flow, all experiments with jets had power law flight behavior. The variance grows superdiffusively for all flows with nontrivial time dependence, except the weakly turbulent flow which appears to approach normal diffusion for very long times, as expected.

Precise verification of the CTRW model is not possible given the experimental limitations. The predictions shown in Fig. 10 for the variance are only correct as $t \to \infty$; for finite t, the variance is composed of several terms. Competition between these terms controls the approach to the asymptotic behavior. These higher order terms can cause the variance to grow faster than its asymptotic growth (γ to appear larger at short times).

There are several reasons that particles are not observable for long periods of time. The most significant reason is probably Ekman pumping [5], a boundary layer effect that results in weak flows that are not perpendicular to the axis of rotation. Particles are illuminated only in a narrow horizontal re-

Table 2. Exponents ν and μ characterizing the power law decay of probability distribution functions for the sticking and flight times, respectively, and the exponent γ for the power law time dependence of the variance of the azimuthal displacement (measured and predicted). A — entry indicates the exponent is undefined.

Flow name	μ	ν	γ_{expt}	γ_{theory}
Time-independent (with six vortices)	—	—	2	2
Seven-vortex (time-periodic)	3.2 ± 0.2	?	~ 1.5	1
Six-vortex (time-periodic)	2.5 ± 0.2	∞	1.65 ± 0.15	1.5
Five-vortex (Eulerian chaos)	?	?	1.55 ± 0.15	1?
Four-vortex (Eulerian chaos)	2.0 ± 0.2	1.3 ± 0.2	~ 1.5	1.3
Weakly turbulent	∞	—	~ 1.2	1

gion, and Ekman pumping provides a small vertical velocity which can move particles into and out of this illuminated slice. Additionally, particles that come too close to the edges of the annulus are lost, although they may be tracked as a new particle if the particle returns to the visible region. A final concern is the non-neutral-buoyancy of the particles; centrifugal effects could cause particles to drift out of the illuminated region. If there are any correlations linking the particle behavior to their longevity in the visible region, this could further affect results. For example, if particles stuck in vortices have a faster vertical drift (perhaps due to Ekman pumping which should be stronger in a vortex), then the observations of long-lived particles will be biased towards flights.

Despite these difficulties, the experiments show that power law scaling and Lévy flights are directly observable in fluid transport. In addition, the diffusive process is clearly anomalous for a broad range of times, and is well described the the continuous time random walk model.

Acknowledgments
We are indebted to Tom Solomon for his role in the initial experiments described in this paper, and also acknowledge helpful discussions with J. Klafter, M. F. Shlesinger, and G. M. Zaslavsky. This work was supported by the Office of Naval Research Grant No. N00014-89-J1495. ERW acknowledges the support of an ONR Augmentation Award for Science and Engineering Training.

References

[1] For reviews, see J. Klafter, M. F. Shlesinger, G. Zumofen, Beyond Brownian motion, Physics Today **49**, 33 (Feb. 1996); M. F. Shlesinger, G. M. Zaslavsky, J. Klafter, Strange kinetics, Nature **363**, 31 (1993); E. W. Montroll and M. F. Shlesinger, in *Nonequilibrium Phenomena II: From Stochastics to Hydrodynamics*, Studies in Statistical Mechanics, Vol. II, eds. J. L. Lebowitz and E. W. Montroll (North-Holland, Amsterdam, 1984), 1.

[2] L. F. Richardson, Atmospheric diffusion shown on a distance-neighbour graph, Proc. Roy. Soc. (London) Ser. A **110** (1926) 709.

[3] T. H. Solomon and J. P. Gollub, Passive transport in steady Rayleigh-Bénard convection, Phys. Fluids **31**, 1372 (1988).

[4] H. Aref, Stirring by chaotic advection, J. Fluid Mech. **143**, 1 (1984).

[5] J. Pedlosky, *Geophysical Fluid Dynamics*, 2nd ed. (Springer-Verlag, New York, 1987).

[6] J. Sommeria, S. D. Meyers and H. L. Swinney, in *Nonlinear Topics in Ocean Physics*, ed. A. Osborne (North-Holland, Amsterdam, 1991), p. 227.

[7] J. Sommeria, S. D. Meyers, and H. L. Swinney, Laboratory simulation of Jupiter's Great Red Spot, Nature **331** (1988) 689.

[8] J. Sommeria, S. D. Meyers, and H. L. Swinney, Laboratory model of a planetary eastward jet, Nature **337** (1989) 58.

[9] T. H. Solomon, E. R. Weeks, H. L. Swinney, Observation of anomalous diffusion and Lévy flights in a two-dimensional rotating flow, Phys. Rev. Lett. **71**, 3975 (1993).

[10] T. H. Solomon, E. R. Weeks, H. L. Swinney, Chaotic advection in a two-dimensional flow: Lévy flights and anomalous diffusion, Physica D **76**, 70 (1994).

[11] E. R. Weeks, T. H. Solomon, J. S. Urbach, H. L. Swinney, Observation of Anomalous Diffusion and Lévy Flights, in: *Lévy Flights and Related Topics in Physics*, eds. M. F. Shlesinger, G. M. Zaslavsky and U. Frisch (Springer-Verlag, Heidelberg, 1995) pp. 51.

[12] E. R. Weeks, J. S. Urbach, H. L. Swinney, Anomalous diffusion in asymmetric random walks with a quasi-geostrophic flow example, Physica D **97**, 219 (1996).

[13] M. S. Pervez and T. H. Solomon, Long-term tracking of neutrally buoyant tracer particles in two-dimensional fluid flows, Exp. Fluids **17**, 135 (1994).

[14] T. H. Solomon, W. J. Holloway, H. L. Swinney, Shear flow instabilities and Rossby waves in barotropic flow in a rotating annulus, Phys. Fluids A **5**, 1971 (1993).

[15] I. Mezic and S. Wiggins, On the dynamical origin of asymptotic t^2 dispersion of a nondiffusive tracer in incompressible laminar flows, Phys. Fluids **6**, 2227 (1994).

[16] D. del-Castillo-Negrete, Asymmetric transport and non-Gaussian statistics of passive scalars in vortices in shear, submitted to Phys. Fluids (1997).

[17] M. F. Shlesinger, Asymptotic solutions of continuous-time random walks, J. Stat. Phys. **10**, 421 (1974).

[18] J. Klafter and G. Zumofen, Lévy Statistics in a Hamiltonian System, Phys. Rev. E **49**, 4873 (1994).

[19] G. I. Taylor, Diffusion by continuous movements, Proc. Lon. Math. Soc. 2 **20**, 196 (1921).

[20] W. Feller, *An Introduction to Probability Theory and Its Applications*, (John Wiley & Sons Inc., New York, 1966) Vol. 2, Chap XVI.8, p. 525.
[21] M. F. Shlesinger, Comment on "Stochastic process with ultraslow convergence to a Gaussian: The truncated Lévy flight", Phys. Rev. Lett. **74**, 4959 (1995).
[22] S. Venkataramani, T. M. Antonsen, E. Ott, Anomalous diffusion in bounded temporally irregular flows, Physica D, to appear.
[23] S. Venkataramani, T. M. Antonsen, E. Ott, Lévy flights in fluid flows with no Kolmogorov-Arnold-Moser Surfaces, Phys. Rev. Lett. **78**, 3864 (1997).
[24] J. P. Bouchaud and A. Georges, Anomalous diffusion in disordered media: statistical mechanisms, models and physical applications, Phys. Rep. **195**, 127 (1990).